Wide-Field In Vivo Confocal Microscopy of Meibomian Gland Acini and Rete Ridges in the Eyelid Margin

Scott Zhou and Danielle M. Robertson

The Department of Ophthalmology, University of Texas Southwestern Medical Center, Dallas, Texas, United States

PURPOSE. In vivo confocal microscopy (IVCM) has been widely used to evaluate changes in the meibomian glands (MGs) in response to age and disease. This study examined the structures described as MGs using wide-field IVCM and laser scanning confocal microscopy (LSCM) in situ and characterized their spatial distribution and localization relevant to the eyelid margin.

METHODS. IVCM was performed on 30 subjects aged 18 to 38 to visualize structures in the eyelid margin. Size, shape, and distribution characteristics were measured, and individual frames were montaged into wide-field images. Structures observed on IVCM were then visualized using LSCM of whole-mount and cryosectioned cadaver eyelids stained with Nile red, mucin-1 (MUC1), laminin-5, and 4′,6-diamidine-2′-phenylindole dihydrochloride.

RESULTS. The size, distribution, and staining patterns of the reflective structures seen on IVCM did not correspond to the MGs in cadaver eyelids. Instead, staining profiles indicated that these structures corresponded to the rete ridges present at the dermal–epidermal junction. Wide-field imaging showed a densely populated field of rete ridges with distinct size and shape characteristics depending on their location relative to the meibomian orifices. A distal shift of the mucocutaneous junction (MCJ) was evident in some eyelids.

CONCLUSIONS. IVCM is unable to visualize MGs in the human eyelid margin due to light attenuation at that tissue depth. LSCM confirms that these structures are rete ridges located at the dermal–epidermal junction. Alterations in the structure of the dermal–epidermal junction within the eyelid margin indicate a shifting of the MCJ and may impact tear film dynamics.

Keywords: meibomian gland, rete ridges, confocal microscopy, eyelid, dry eye

Dry eye disease (DED) is a common ophthalmic condition caused by decreased tear production or accelerated tear evaporation. The prevalence of DED is estimated to be 16 million in the US population.[1] Symptoms include irritation, redness, and easily fatigued eyes, and can be exacerbated by various factors, such as dry conditions, contact lens wear, or computer use.[2] DED can predispose patients to other ophthalmic conditions such as recurrent corneal erosions and infection, and in severe cases, corneal scarring can occur with gradual loss of vision.[3]

Meibomian glands (MGs) are specialized holocrine sebaceous glands located on the inner margin of the tarsal plates. Their primary function is to produce meibum, a compositionally complex lipid secretion that promotes tear film stability and prevents evaporation.[4] Meibomian gland dysfunction (MGD), characterized by impaired meibum delivery due to obstruction, inflammation, gland dropout, and so on, is believed to be one of the most common disorders encountered in ophthalmic practice and the leading cause of DED.[5,6] Thus, a better understanding of MGD pathology may reveal pathogenic mechanisms and, ultimately, lead to better treatment paradigms for patients with evaporative dry eye.

In vivo confocal microscopy (IVCM) is a noninvasive technique that offers cellular resolution of the cornea, conjunctiva, and eyelid margin, and is useful in the examination and diagnosis of ocular pathology.[7,8] Kobayashi, Yoshita, and Sugiyama[9] published the first study to use IVCM to view the hyperreflective, weblike structures in the eyelid margin that were presumed to be MGs. Over the past decade, these structures have been studied as MGs, with most studies focusing on changes in size, shape, and reflectance as markers of MGD.[10-16] Surprisingly, no study to date has positively confirmed the identity of these structures.

In the present study, we used multiple imaging modalities to characterize the location and structure of MGs in human eyelids in vivo and in cadaver eyelids in situ. We identified the presence of laminin-5 and absence of mucin-1 (MUC1) within the structures found on IVCM using laser scanning confocal microscopy (LSCM). These findings indicate that the structures previously reported as MGs by IVCM are instead rete ridges of the dermal–epidermal barrier at the eyelid margin. We then used wide-field IVCM imaging to characterize changes in size and shape of these ridges across the eyelid margin and found evidence of migration of the mucocutaneous junction (MCJ) in human subjects.

METHODS

Study Design and Subject Recruitment

This is a cross-sectional study investigating the reflective structures visible in the eyelid margin using IVCM. Patients were recruited from the University of Texas (UT) Southwestern campus and the surrounding community as part of a larger, prospective clinical trial, NCT02347631. All procedures were approved by the Institutional Review Board at UT Southwest-

ern Medical Center and adhered to the Declaration of Helsinki. All volunteers signed a written informed consent prior to participation in the study.

Inclusion criteria for this study included any nonpregnant adult between the ages of 18 and 38 years without any evidence of existing ocular or systemic disease and no concurrent use of any topical ophthalmic medications. Volunteers with a history of keratorefractive surgery, DED, or infectious disease were excluded. All volunteers were either non-contact lens wearers or contact lens wearers who had not worn contact lenses for a minimum of 30 days prior to the IVCM evaluation (washout period). Before initiating the 30-day washout period, all volunteers underwent a comprehensive ocular examination including a biomicroscopic examination of the cornea and eyelid margin and a dilated fundus examination to rule out any ocular pathology. Height of the inferior tear meniscus was measured using parallelepiped illumination and the standard slit-lamp scale. The cornea was further evaluated for staining using 2 μL 2.0% nonpreserved fluorescein (Greenpark Pharmacy, Houston, TX, USA), which was instilled onto the superior bulbar conjunctiva of both eyes. Fluorescein staining was graded according the National Eye Institute scale for corneal staining in five regions using a scale of 0 to 3. For all fluorescein-based measurements, a yellow #12 filter (Tiffen, Hauppauge, NY, USA) was used. As the last clinical test, tear production was assessed using a Schirmer's tear test without anesthesia. The Schirmer strip (Alcon Laboratories, Ft. Worth, TX, USA) was placed in the lower fornix near the lateral canthus, and the subject was instructed to close his or her eyes. The length of the wetted area after 5 minutes was measured. All tests were performed for both eyes, and the values for the right and left eyes were averaged to achieve a final measurement. Per study protocol, all volunteers were examined between 8 AM and 12 PM.

In Vivo and In Situ Clinical Confocal Microscopy

For human clinical imaging, one drop of proparacaine (Alcon Laboratories, Fort Worth, TX, USA) was instilled into each eye. Immediately prior to imaging, eyelids were everted using a cotton-tipped applicator. For human cadaver eyelid imaging, eyelids were excised from 1-day postmortem cadavers obtained from the Willed Body Program at UT Southwestern Medical Center. Excised eyelids were scanned by IVCM and then immediately fixed as described below. In vivo confocal microscopy was performed using an HRT II with Rostock Cornea Module (Heidelberg Instruments, Heidelberg, Germany) modified for remote-controlled scanning and real-time image streaming. The details of image acquisition are described elsewhere.[17,18] A clear plastic confocal cap was optically coupled to the objective with Systane Gel (Alcon Laboratories) and then used to applanate the center of the upper eyelid margin. Five to 10 scans per eyelid were streamed in real time and saved to an external hard drive as volume files. Volume files were then opened in MetaMorph Software (Molecular Devices, Sunnyvale, CA, USA), and single image frames (400 × 400 μm) were extracted and subsequently compiled in Microsoft PowerPoint (Microsoft Corporation, Redmond, WA, USA) to form wide-field images.

Reagents for In Situ Imaging

The following antibodies were used in this study: a mouse anti-laminin 5 (sc-13586; Santa Cruz Biotech, Santa Cruz, CA, USA), rabbit anti-MUC1 (14161S; Cell Signaling, Danvers, MA, USA), Alexa Fluor 488–conjugated goat anti-rabbit (4412S, Cell Signaling), and Alexa Fluor 647–conjugated goat anti-mouse (4410S, Cell Signaling). 4′,6-Diamidine-2′-phenylindole dihy-

drochloride (DAPI, Cell Signaling) and Nile red (Thermo Fisher Scientific, Waltham, MA, USA) were used to label nuclei and lipid, respectively.

Immunofluorescence

Immediately after IVCM, samples were fixed in 4% paraformaldehyde (PFA; Electron Microscopy Sciences, Hatfield, PA, USA) for 30 minutes at room temperature. Fixed samples were embedded in Tissue-Tek O.C.T. compound (Sakura Finetek, Torrance, CA, USA) at −20°C and subsequently cut into 20-μm-thick sections using a Leica CM3050S research cryostat (Leica, Wetzlar, Germany). For immunofluorescence studies, whole-mount and cryosectioned samples were blocked in 1% bovine serum albumin (BSA; Sigma-Aldrich Corp., St. Louis, MO, USA) containing 0.3% Triton X (TX)-100 in phosphate-buffered saline (PBS) for 1 hour before incubation in primary antibodies. Primary antibodies were diluted in 0.5% BSA and 0.1% TX-100 in PBS at 4°C overnight. As a negative control for staining, parallel samples were incubated in 0.5% BSA and 0.1% TX-100 in PBS without primary antibody. Samples were then washed three times in 0.3% TX-100, and incubated in secondary antibodies with fluorescent probes to label nuclei and/or lipid for 2 hours at room temperature. Samples were again washed three times in 0.3% TX-100. Whole-mount tissue samples were mounted on MatTek coverslip bottom culture dishes (MatTek Corporation, Ashland, MA, USA) in 100 μL 75% glycerol in PBS. For cryosections, one drop of Vectashield mounting medium (Vector Labs, Burlingame, CA, USA) was added; sections were coverslipped and sealed prior to imaging.

Laser Scanning Confocal Microscopy

For in situ laser scanning confocal imaging of whole-mount and cryosectioned eyelids, LSCM was performed using a Leica SP8 confocal microscope (Leica Microsystems, Buffalo Grove, IL, USA). The microscope is equipped with a motorized scanning stage to allow for mosaic imaging. Sequential scanning was performed to minimize spectral overlap between channels. The following lasers were used for scanning: a UV laser for excitation of DAPI, a 488-nm laser for excitation of Alexa Fluor 488, 561 nm for excitation of Nile red, and 633 nm for reflectance imaging and excitation of Alexa Fluor 647. For whole-mount imaging, Z-stacks were acquired with a 0.2-μm step size. Image stacks were reconstructed three-dimensionally using Imaris 7.3.1 (Bitplane, Concord, MA, USA) and are presented as maximum-intensity projections. For cryosections, images were collected using the stitch function in the Leica Application Suite Advanced Fluorescence software. Adjacent regions were automatically stitched to create a large, two-dimensional wide-field image of the eyelid.

Image Analysis

For morphometric analysis of the eyelid structures, area, perimeter, and distance measurements were performed using MetaMorph software. Circularity of the structures in the in situ confocal images and in the IVCM images was measured with the formula $C = 4\pi(\text{area}/\text{perimeter}^2)$, with $C = 1$ indicating a perfect circle and C approaching 0 indicating an increasingly elongated shape.

Statistical Analysis

All data are expressed as mean ± standard deviation. For comparison between two groups (such as sex and ethnicity), a Student's *t*-test was used. To test for differences across multiple groups, a 1-way ANOVA was performed using SigmaPlot 12.5
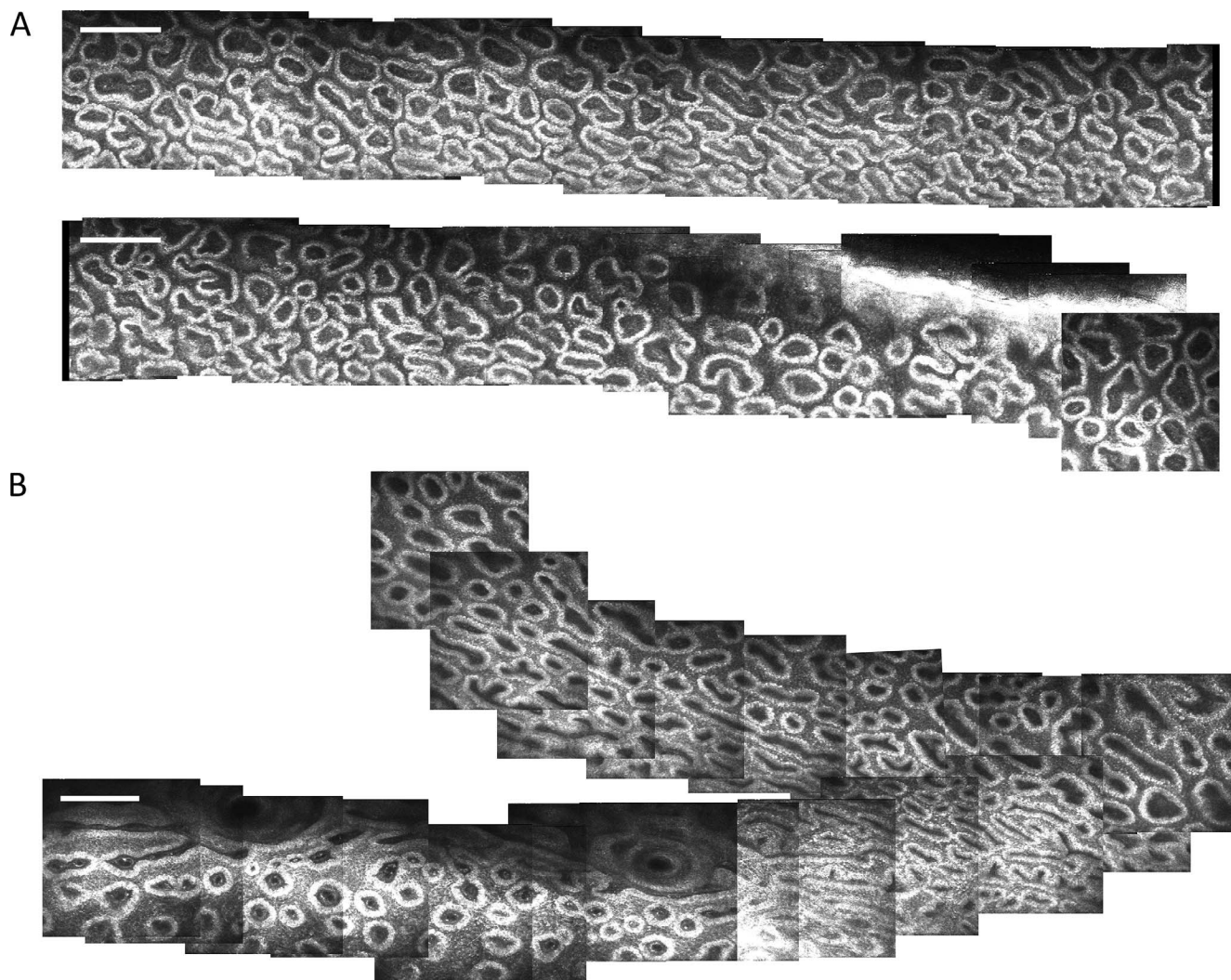
A

B

FIGURE 1. Wide-field imaging of the palpebral epithelium at the free lid margin. (**A**) Wide-field imaging shows a large field of densely arranged ring-like structures that span horizontally across the upper eyelid margin. *Bottom* in (**A**) is a continuation of the *top* in (**A**). (**B**) Distinct regions relative to the meibomian orifice can be seen, distinguished by characteristic differences in size and shape of the structures. *Scale bar*: 200 µm.

(Systat Software, San Jose, CA, USA). A Shapiro-Wilk test was used to test for a normal distribution. For normally distributed data, a 1-way ANOVA was performed with a Holm-Sidak post hoc multiple comparison test. For nonnormally distributed data, the Kruskal-Wallis test by ranks was performed with Dunn's test for multiple comparisons. To test for a correlation between age and circularity within the different lid regions, a Pearson's correlation coefficient was used. $P < 0.05$ was considered to be statistically significant.

RESULTS

The mean age of volunteers recruited in this study was 27.1 ± 5.2 years (range, 19–38). The majority of volunteers were female (77% female compared to 23% male). Forty percent of volunteers were Asian, 30% were Caucasian, and 30% were African American. Eighty percent of volunteers self-reported as non-Hispanic compared to 20% who self-reported as Hispanic. There were no differences in any of the measured parameters for sex, race, or ethnicity. At the initial screening visit, all volunteers were healthy adults with no evidence of any existing ocular pathology. None of the volunteers presented

with clinically significant corneal staining or inspissated or inflamed MGs. Mean tear film height for all participants was 0.19 ± 0.06 mm with a mean Schirmer's test measurement of 22.4 ± 8.7 mm. None of the patients reported any dry eye symptoms at the time of examination.

Wide-field imaging of the structures on IVCM with a 670-nm wavelength laser revealed a large field of densely distributed structures characterized by a hyperreflective border with a hyporeflective center localized in the vicinity of the meibomian orifices (Fig. 1A). As the imaging depth increased from 20 to 100 µm below the epithelial surface, these structures appeared to grow and merge with each other until light attenuation prevented further viewing.

In a single 400×400-µm frame, there were an average of 30 to 40 circular/ovoid-shaped structures depending upon the region viewed and the geographical location within the MCJ. The size and shape of these structures varied significantly depending on their location (Fig. 1B). As shown in Figures 1 and 2, distinct regions across the eyelid margin were visible by IVCM. Within the periorificial region, immediately above and below the meibomian orifices, the structures were thin and elongated, running horizontally between orifices with small, densely packed structures filling the bulk of the area (Fig. 2B).
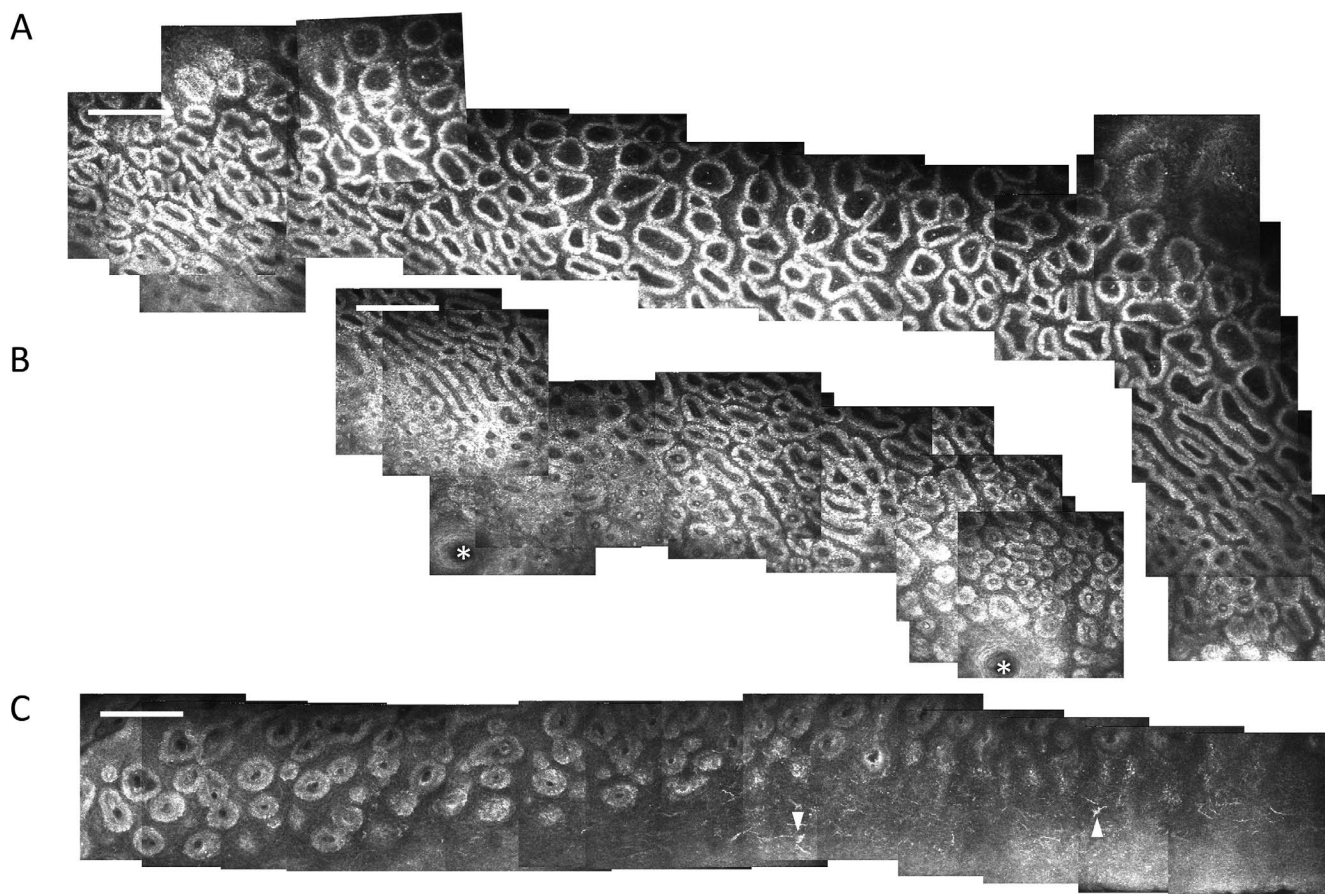
FIGURE 2. Representative wide-field IVCM images of the distinct regions within the eyelid margin. (**A**) The free lid margin; (**B**) the periorificial region; and (**C**) the MCJ and lid wiper regions. *Scale bar*: 200 μm. *Asterisks* mark meibomian orifices, *arrowheads* mark presumed dendritic cells at the start of the lid wiper region.

Moving above this region farther into the free lid margin, the structures became larger, less tortuous, and less densely packed (Fig. 2A). The structures were relatively sparse in the MCJ below the orifices, but what structures were present were highly uniform with an extremely circular shape. In the lid wiper region beneath the MCJ, these structures were completely absent; occasional cells that were dendritic in appearance were found in this region instead (Fig. 2C). To examine the interregional differences in the structures of interest, area and circularity were calculated for the periorificial region, the free lid margin, and the MCJ. As shown in Figure 3A, the area of the structures viewed by IVCM ranged from 1063.4 ± 0.11 μm^2 up to 2983.8 ± 0.05 μm^2 depending on the region of interest. There were significant differences in the area of the reflective structures between the periorificial region and the free lid margin ($P < 0.05$) and between the periorificial region and the MCJ ($P < 0.05$, Fig. 3A). Circularity of the reflective structures differed between all three regions ($P < 0.001$, Fig. 3B). There was a significant correlation between age and the circularity of the structures in the periorificial region ($P < 0.00$, Fig. 3C).

Interestingly, the location of the MCJ relative to the meibomian orifices varied between individuals. In most individuals, the densely packed structures of the periorificial region completely surrounded the meibomian orifices from above and below (Fig. 4A). In some individuals, however, these structures failed to surround the orifices from below, with the MCJ encroaching into the periorificial region (Fig. 4B).

Cryosectioned tissue from cadaver eyelids stained for MUC1 demonstrated the spatial distribution of MG acini beneath the palpebral conjunctiva (Figs. 5A, 5B). Staining for Nile red revealed that the meibomian acinar lumens were filled with free lipid (Fig. 5C). Using the cryostat-sectioned images, we calculated the average area of the acini and the distance of the acini from the eyelid margin. This allowed for a direct comparison between the structures observed on IVCM and the confirmed MG acini in the in situ eyelid tissue. Using these images, we determined that the mean area for MG acini was $33,487 \pm 17,699$ μm^2 ($n = 46$). This was more than an order of magnitude larger than the structures visible on IVCM. The acini closest to the MCJ were on average 417 ± 70 μm ($n = 8$) from the epithelial surface, with no acini being closer than 300 μm.

In contrast to this, the circular/ovoid-like structures viewed on IVCM were probed at a depth between 20 and 100 μm from the epidermal surface, much shallower than the depth of MG acini. The IVCM used in this study has a wavelength of 670 nm. This allows optical sectioning up to a depth of approximately 100 μm at the free lid margin, after which significant light attenuation prevents further imaging. Importantly, staining for laminin-5, a key component of anchoring fibrils within the dermal–epidermal junction, revealed bright, linear fluorescence immediately beneath the palpebral epithelium corresponding to the epithelial basement membrane (Fig. 5D). The depth of the dermal–epidermal junction from the palpebral surface fell within the range of the structures noted on IVCM.

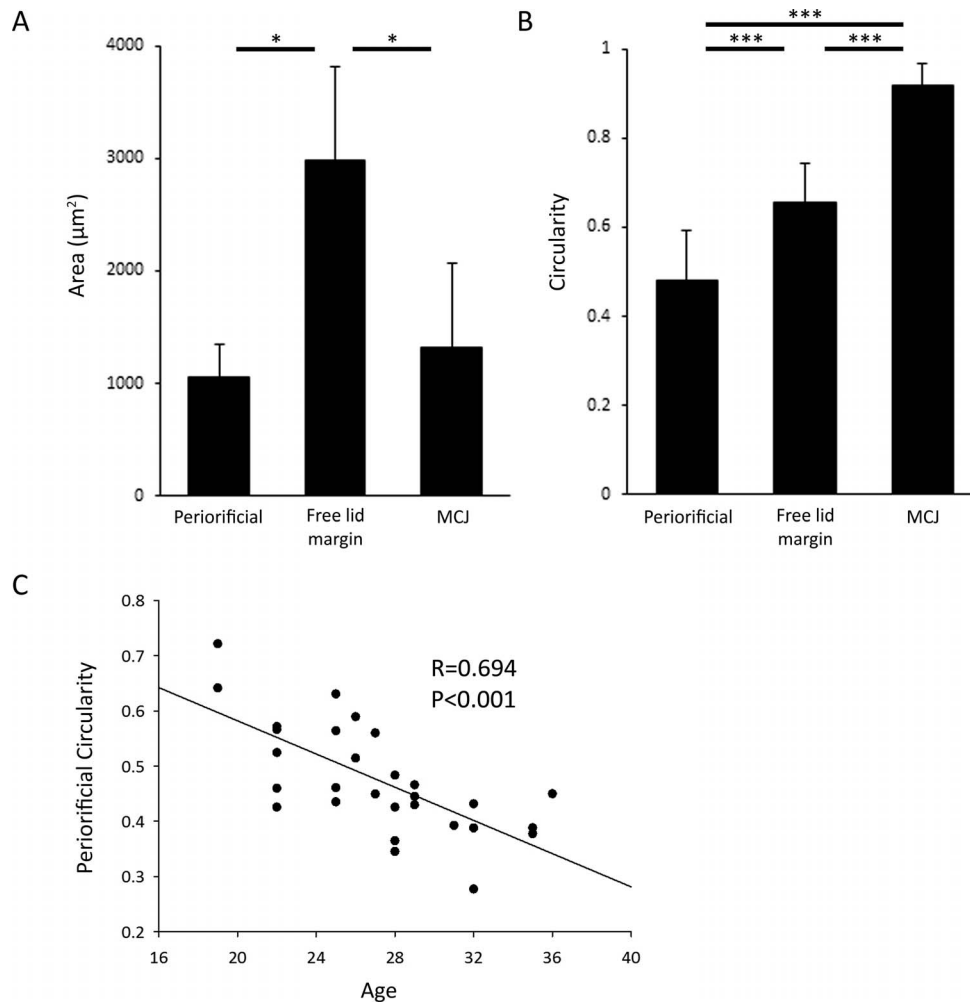Structures analogous to those found on IVCM exam were visible on whole-mount samples in the areas surrounding the

FIGURE 3. Area and circularity measurements of the structures within the periorificial, free lid margin, and MCJ regions. (**A**) The area of the structures in the free lid margin was significantly larger than those in the periorificial and MCJ (*$P < 0.05$, Kruskal-Wallis test by ranks with Dunn's test for multiple comparisons, $n = 30$). (**B**) Structures in the MCJ demonstrated the greatest circularity, whereas structures located in the periorificial region were thin and elongated (***$P < 0.001$, 1-way ANOVA with Holm-Sidak post hoc multiple comparison test, $n = 30$). (**C**) There was a significant correlation between age and circularity of the structures within the periorificial region (Pearson's correlation coefficient, $R = 0.694$, $P < 0.001$).

meibomian orifices via reflectance imaging using LSCM (Fig. 6A). These structures were characterized by a hyperreflective ring surrounding a hyporeflective center, similar to those seen on IVCM. The morphologic appearance of these structures varied somewhat from the in vivo images due to postmortem tissue changes and the absence of any lid tension in situ. The postmortem changes were also visible on in situ eyelids scanned by IVCM; however, there was little contrast in the postmortem tissue, which made imaging difficult (data not shown). Laminin-5 staining revealed a thin basement membrane tightly associated with the structures with no associated MUC1 staining (Fig. 6B). This basement membrane was found lining the border between the hyperreflective and hyporeflective regions. Nile red lipid staining showed hyperintense fluorescence of meibum present within the meibomian orifice, with no comparable staining within the structures (Fig. 6C). A three-dimensional (3D) reconstruction of a z-stack with *XZ* and *YZ* orthogonal views of laminin-5 showed that the basement membrane was highly undulating, forming ridges of invaginations between the epithelium and deeper tissue (Figs. 7A–C). A representative *XY* image showed that the rete ridges took on a circular appearance when viewed within a single image plane.

DISCUSSION

This study reports the first characterization of the dermal–epidermal junction in the eyelid margin using IVCM of human subjects and LSCM of MGs in situ. The dermal–epidermal junction at the level of the MCJ is readily visible on a clinical confocal exam. It is characterized as the collection of acinar-like structures with a hyperreflective epithelial layer surrounding a hyporeflective luminal center. These structures appear only in the immediate vicinity of the meibomian orifices, with a maximum density surrounding the orifices and eventually disappearing when viewed too far above or below the level of the orifice openings.

Prior histologic studies have shown that there are approximately 10 to 15 acini per MG, with 40 MGs across the entire upper eyelid.[19] Based upon the appearance of human MGs in cross-sectioned tissue, they further showed that the acini are approximately 150 to 200 μm in diameter,[19] corresponding to an area of approximately 30,000 μm². This finding is in agreement with the area of MG acini calculated from cryostat-sectioned tissue in our study. In contrast to this, the area of the structures visible in the eyelid margin using IVCM was an order of magnitude smaller than the area of the MG acini. Moreover,
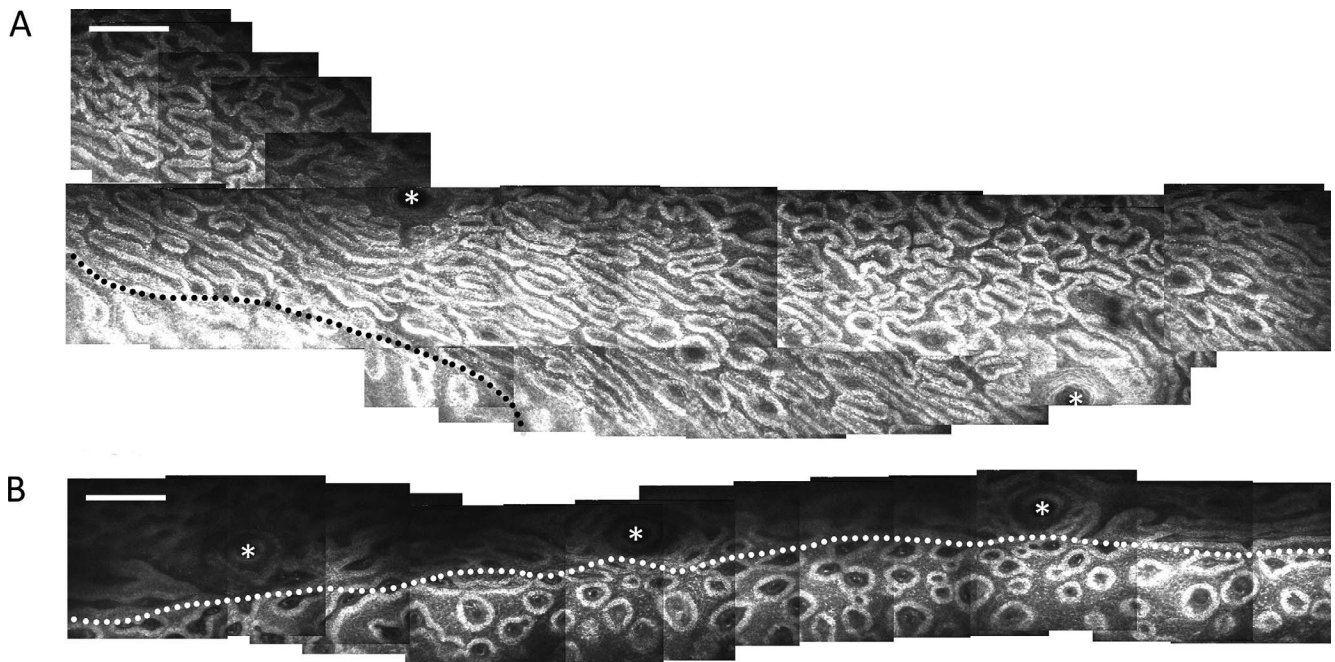
FIGURE 4. Wide-field IVCM imaging highlighting the level of the MCJ region relative to the meibomian orifices. (**A**) The border of the MCJ region (*dotted line*) was observed below the meibomian orifices (*asterisks*), which were surrounded by the periorificial region in many subjects. (**B**) In some eyelids, the MCJ region encroached into the level of the meibomian orifices, representing an anterior shift of the MCJ. *Scale bar*: 200 µm.

infrared meibography of the spatial distribution of MGs shows distinct, prominent, regular spacing between each gland.[20] This contrasts with our wide-field images that revealed a vast array of these structures with no obvious interglandular spacing arrangement between the meibomian orifices.

In addition to the horizontal spatial distribution, previous studies have determined that the excretory duct of the MG extends approximately 0.5 mm beneath the epidermis of the free lid margin before reaching MG acini.[19] This is also in agreement with our present findings. When considering the depth of the MG acini based upon their proximity to the eyelid margin, it is important to take into account the optical properties of the IVCM. In contrast to the IVCM that has a 670-nm laser and can penetrate approximately 100 µm into the
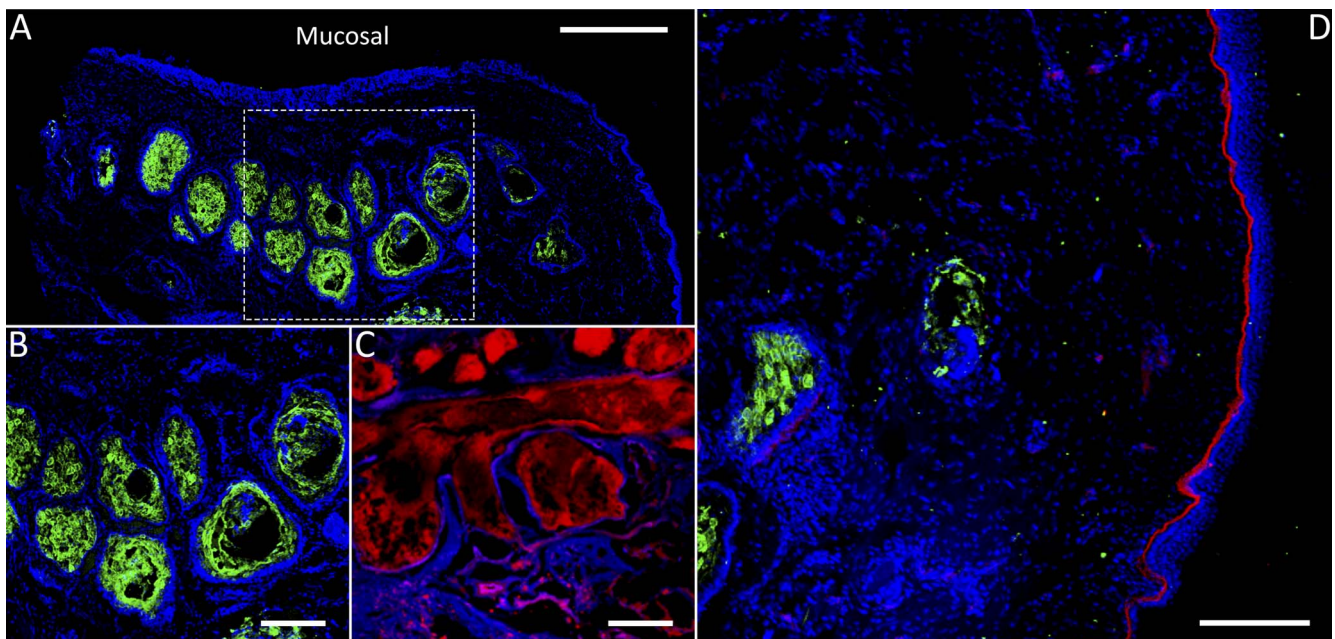

FIGURE 5. LSCM images of meibomian gland cryosections. (**A**) MUC1 staining (*green*) reveals meibomian gland acini linearly arranged beneath the mucosal epithelium (*arrowhead*). Nuclei counterstained with DAPI (*blue*). *Scale bar*: 500 µm. (**B**) An enlarged image (identified by the *dotted boxed area*) from (**A**). *Scale bar*: 200 µm. (**C**) Nile red staining shows free lipids within the meibomian gland acini. *Scale bar*: 200 µm. (**D**) Laminin-5 staining (*red*) reveals a thin region of fluorescence staining immediately beneath the epithelial surface of the free lid margin, corresponding to the basement membrane. *Scale bar*: 200 µm.
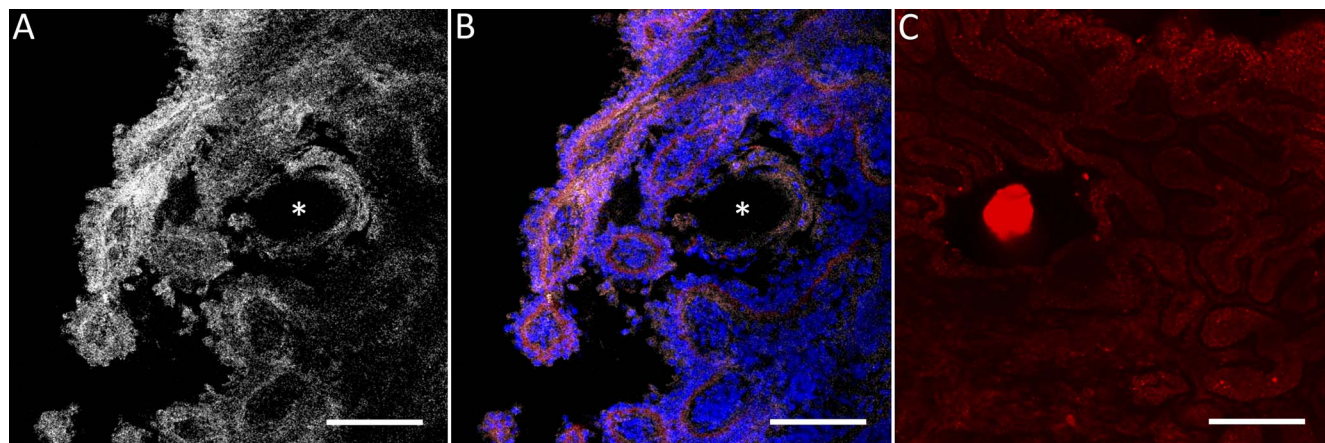
FIGURE 6. LSCM en face images of whole-mount cadaver eyelid tissue near the meibomian orifices. (**A**) Reflectance imaging using a 633-nm wavelength revealed ring-like structures analogous to those seen on IVCM (*asterisk* indicates the meibomian orifice). (**B**) Overlay with DAPI and laminin-5 staining shows that these structures are intimately associated with the epithelial basement membrane (*asterisk* indicates the meibomian orifice). (**C**) Nile red staining of a different tissue section shows the presence of meibum within the meibomian orifice, with no comparable staining within the surrounding structures. *Scale bar*: 100 μm.

eyelid, a much longer wavelength is required for deep penetration into skin. Studies on confocal imaging in human skin report using lasers that range from 800 up to 1064 nm.[21] Importantly, a wavelength of 830 nm has been shown to reach a penetration depth of approximately 200 up to 250 nm.[21] This wavelength is much longer than the wavelength in the commercially available in vivo confocal microscopes that are widely used in ophthalmology and is still not sufficient to reach the depth required to discern any features of the MGs.

Likewise, the localizations of Nile red and MUC1 as viewed by fluorescent confocal microscopy of the MG acini and the IVCM structures are also discordant. Nile red is a lipophilic stain for intracellular lipids. MG cryosections showed a bright

Nile red signal within some of the acinar lumens, corresponding to secreted meibum. Whole-mount samples showed a similarly bright Nile red signal within the MG orifices corresponding to meibum secreted by the MGs. However, we did not detect this level of staining within the circular/ovoid structures previously reported as MGs. MUC1 is a membrane-associated glycoprotein highly expressed by mucosal epithelium and glands, including the MGs.[22,23] In human MG cryosections, MUC1 localized within the MG acini, whereas 3D analysis of whole-mount human eyelids failed to show any MUC1 staining in the region where the circular/ovoid structures are found on IVCM. Taken together, these studies
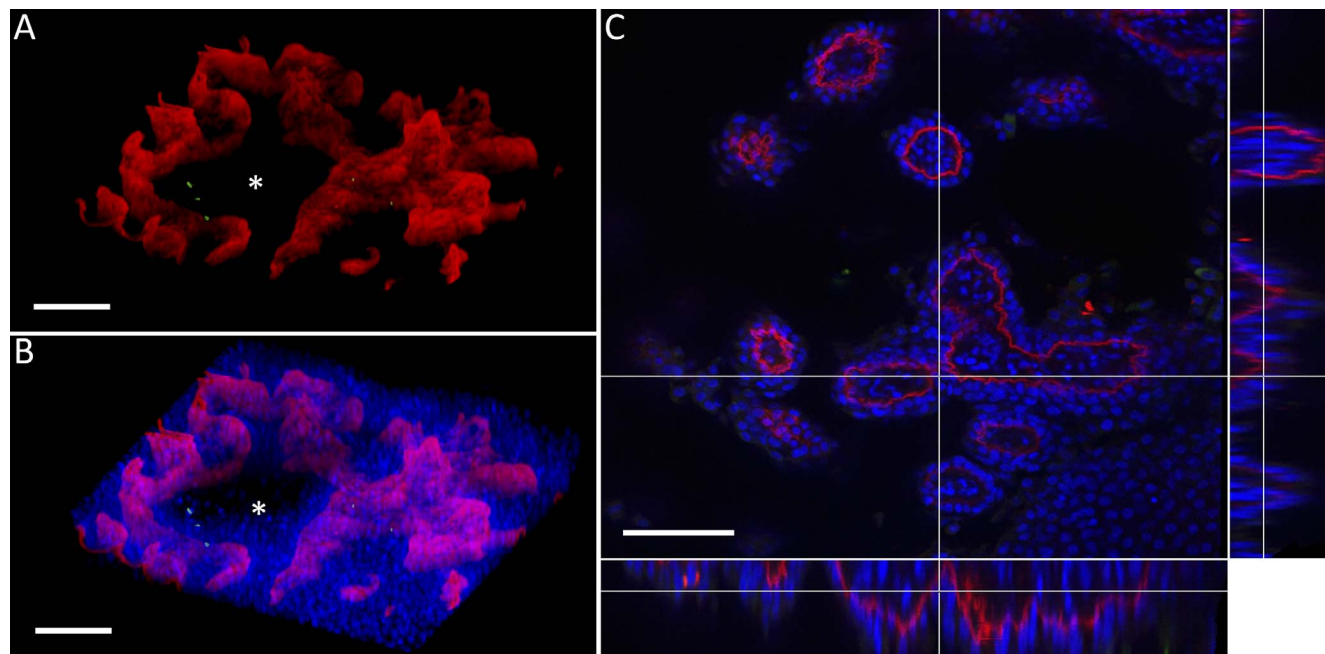

FIGURE 7. Maximal-intensity projection of laminin-5 and MUC1 staining in the eyelid margin. (**A**) 3D reconstruction of laminin-5 (*red*)–stained tissue shows a basement membrane with marked undulations between the dermis and epidermis. An *asterisk* denotes the area of the meibomian orifice. There was no MUC1 (*green*) staining at the dermal–epidermal junction. (**B**) Overlay with DAPI (*blue*) confirms that the undulating laminin-5 staining surrounds the meibomian orifice (*asterisk*). (**C**) Orthogonal *XZ* and *YZ* images showing the undulating laminin-5 staining corresponding to circular regions within the *XY* plane. *Scale bar*: 100 μm.

support the argument that the IVCM structures present in the lid margin are not MG acini as previously reported.[10-16]

Dermatologic IVCM studies using an infrared laser in several areas of the body show similar structures that have been identified as rete ridges of the dermal–epidermal junction.[24,25] These studies include those of dermatologic lesions of the human eyelid.[26] Using laminin-5, a key component of anchoring fibrils within the dermal–epidermal junction, we labeled the rete ridges in the human eyelid in situ.[27] Importantly, we found a tight association between the location of the basement membrane of the epidermis and IVCM structures of interest at the border between the hyper- and hyporeflective zones. We further confirmed that the basement membrane was immediately beneath the epidermal surface of the free lid margin, within the ~100-μm depth visible on IVCM. Collectively, our histologic measurements and immunofluorescence labeling studies provide strong evidence to support the conclusion that the previously labeled MGs seen with IVCM are not MGs, but are rete ridges in the dermal–epidermal junction, with the hyperreflective border representing the stratum basale of the epidermis and the hyporeflective center representing the superficial dermis. Rete ridges are fewer and less pronounced in most nonkeratinized mucosal surfaces, which may explain why they are not found below the level of the MCJ.[28] They are optimally visible at the level of the orifices, the region of the cutaneous epidermis where the keratinized layer is the thinnest. Moving farther upward into the free lid margin, the keratinized layer thickens, preventing penetration of the 670-nm IVCM laser deep into the tissue due to significant light attenuation.

The rete ridges form invaginations at the dermal–epidermal junction that serve to increase the contact area between the two layers, thus strengthening their adhesion and scattering the external forces to which they are exposed.[29] Three-dimensional volume reconstruction of laminin-5 staining shows the basement membrane undulating between the dermis and the epidermis. In addition, virtual sectioning in the *XY* plane shows shapes that range from circular and structured to elongated and irregular. Structures that are isolated and distinct can be seen at the peaks of the ridges, but moving deeper toward their base causes the structures to shift and merge, similar to what is seen on IVCM.

Using quantitative image analysis, we were able to calculate a morphologic profile of the rete ridges, based upon area and circularity, within the distinct regions observed on IVCM. We speculate that the measured differences in area and shape of the rete ridges within these regions may reflect the specific types of mechanical forces encountered. The skin at the level of the orifices represents the cutaneous membrane of the eyelid that is closest to the lid wiper region. It is likely that the primary mechanical stress this region experiences is the vertical shear force produced as the eyelid and the globe slide past each other during the action of blinking and from eyelid rubbing. It is possible that the rete ridges at this level form elongated structures running horizontally between orifices to maximize the strength of the junction against vertical shear. Moving farther into the free lid margin, the structures become more circular and oblong in shape, possibly reflecting that the forces on the cutaneous surface become less unidirectional the farther the distance from the lid wiper region.

The relationship between rete ridge morphology and MGD is unclear. Previous studies have focused on morphologic differences in rete ridges, albeit mislabeled as MG acini, between subjects with MGD and controls.[10-16] However, our study shows that, even within an individual, the location of the rete ridges significantly impacts key characteristics such as size, shape, and brightness on IVCM; it is unclear if this factor was accounted for in prior studies. Rete ridges are also known to change with age. Reported age-related changes include reduction in both depth and interdigitation indices.[30,31] Consistent with these prior studies, we also found a change in the rete ridges in the periorificial region that was correlated with age. While the functional significance of these changes is not yet clear, they may underlie the previous IVCM reports of MG atrophy and dropout. Further studies will be needed to clarify these findings.

Past studies have also shown an anterior displacement of the MCJ in the context of MGD in both human and animal models.[32-36] Though the relationship between the two is also unclear, it has been suggested that the displacement may affect the contact between the eyelid and the ocular surface, leading to altered tear film dynamics.[37] Notably, several studies have found that this shift was significantly correlated with the quality and quantity of MG secretions.[33,34] In our study, we were able to find evidence of displacement of the MCJ in certain individuals based on the IVCM morphology of rete ridges alone. These findings suggest that IVCM of the rete ridges in the palpebral margin can be used to monitor changes to the epidermal surface and that the shift in the MCJ may play a role in tear film dynamics and DED. Further studies correlating these changes with clinical symptoms are needed.

In conclusion, the morphologic and immunohistochemical characteristics of the structures previously reported as MG acini on IVCM of the palpebral lid margin confirm that these structures are rete ridges in the dermal–epidermal junction. They show distinct morphologies depending on their location, which can be used to identify the MCJ and adjacent skin regions. This updated interpretation may provide new insight into the role of palpebral surface changes in MG dysfunction and dry eye.

References

1. Farrand KF, Fridman M, Stillman I, Schaumberg DA. Prevalence of diagnosed dry eye disease in the United States among adults aged 18 years and older. *Am J Ophthalmol*. 2017;182: 90–98.

2. Golden MI, Fries PL. *Dry Eye Syndrome*. Treasure Island, Florida: StatPearls; 2017.

3. Stevenson W, Chauhan SK, Dana R. Dry eye disease: an immune-mediated ocular surface disorder. *Arch Ophthalmol*. 2012;130:90–100.

4. Chhadva P, Goldhardt R, Galor A. Meibomian gland disease: the role of gland dysfunction in dry eye disease. *Ophthalmology*. 2017;124:S20–S26.

5. Geerling G, Baudouin C, Aragona P, et al. Emerging strategies for the diagnosis and treatment of meibomian gland dysfunction: Proceedings of the OCEAN group meeting. *Ocul Surf*. 2017;15:179–192.

6. Lemp MA, Crews LA, Bron AJ, Foulks GN, Sullivan BD. Distribution of aqueous-deficient and evaporative dry eye in a clinic-based patient cohort: a retrospective study. *Cornea*. 2012;31:472–478.

7. Petroll WM, Robertson DM. In vivo confocal microscopy of the cornea: new developments in image acquisition, reconstruction, and analysis using the HRT-Rostock Corneal Module. *Ocul Surf*. 2015;13:187–203.

8. Alhatem A, Cavalcanti B, Hamrah P. In vivo confocal microscopy in dry eye disease and related conditions. *Semin Ophthalmol*. 2012;27:138–148.

9. Kobayashi A, Yoshita T, Sugiyama K. In vivo findings of the bulbar/palpebral conjunctiva and presumed meibomian glands by laser scanning confocal microscopy. *Cornea*. 2005;24:985–988.

10. Matsumoto Y, Sato EA, Ibrahim OM, Dogru M, Tsubota K. The application of in vivo laser confocal microscopy to the diagnosis and evaluation of meibomian gland dysfunction. *Mol Vis*. 2008;14:1263–1271.

11. Villani E, Ceresara G, Beretta S, Magnani F, Viola F, Ratiglia R. In vivo confocal microscopy of meibomian glands in contact lens wearers. *Invest Ophthalmol Vis Sci*. 2011;52:5215–5219.

12. Ibrahim OM, Matsumoto Y, Dogru M, et al. In vivo confocal microscopy evaluation of meibomian gland dysfunction in atopic-keratoconjunctivitis patients. *Ophthalmology*. 2012;119:1961–1968.

13. Agnifili L, Fasanella V, Costagliola C, et al. In vivo confocal microscopy of meibomian glands in glaucoma. *Br J Ophthalmol*. 2013;97:343–349.

14. Fasanella V, Agnifili L, Mastropasqua R, et al. In vivo laser scanning confocal microscopy of human meibomian glands in aging and ocular surface diseases. *Biomed Res Int*. 2016;2016:7432131.

15. Liang H, Randon M, Michee S, Tahiri R, Labbe A, Baudouin C. In vivo confocal microscopy evaluation of ocular and cutaneous alterations in patients with rosacea. *Br J Ophthalmol*. 2017;101:268–274.

16. Agnifili L, Mastropasqua R, Fasanella V, et al. Meibomian gland features and conjunctival goblet cell density in glaucomatous patients controlled with prostaglandin/timolol fixed combinations: a case control, cross-sectional study. *J Glaucoma*. 2018;27:364–370.

17. Petroll WM, Cavanagh HD. Remote-controlled scanning and automated confocal microscopy through focusing using a modified HRT rostock corneal module. *Eye Contact Lens*. 2009;35:302–308.

18. Petroll WM, Weaver M, Vaidya S, McCulley JP, Cavanagh HD. Quantitative 3-dimensional corneal imaging in vivo using a modified HRT-RCM confocal microscope. *Cornea*. 2013;32:e36–e43.

19. Knop E, Knop N, Millar T, Obata H, Sullivan DA. The international workshop on meibomian gland dysfunction: report of the subcommittee on anatomy, physiology, and pathophysiology of the meibomian gland. *Invest Ophthalmol Vis Sci*. 2011;52:1938–1978.

20. Arita R, Fukuoka S, Morishige N. New insights into the morphology and function of meibomian glands. *Exp Eye Res*. 2017;163:64–71.

21. Gonzalez S. Confocal reflectance microscopy in dermatology: promise and reality of non-invasive diagnosis and monitoring. *Actas Dermosifiliogr*. 2009;100:56–69.

22. Hattrup CL, Gendler SJ. Structure and function of the cell surface (tethered) mucins. *Annu Rev Physiol*. 2008;70:431–457.

23. Khandelwal P, Liu S, Sullivan DA. Androgen regulation of gene expression in human meibomian gland and conjunctival epithelial cells. *Mol Vis*. 2012;18:1055–1067.

24. Scope A, Benvenuto-Andrade C, Agero AL, et al. In vivo reflectance confocal microscopy imaging of melanocytic skin lesions: consensus terminology glossary and illustrative images. *J Am Acad Dermatol*. 2007;57:644–658.

25. Braga JC, Macedo MP, Pinto C, et al. Learning reflectance confocal microscopy of melanocytic skin lesions through histopathologic transversal sections. *PLoS One*. 2013;8:e81205.

26. Cinotti E, Perrot JL, Campolmi N, et al. The role of in vivo confocal microscopy in the diagnosis of eyelid margin tumors: reply from the authors. *J Am Acad Dermatol*. 2015;72:e123.

27. Nishiyama T, Amano S, Tsunenaga M, et al. The importance of laminin 5 in the dermal-epidermal basement membrane. *J Dermatol Sci*. 2000;24(suppl 1):S51–S59.

28. Ciano J, Beatty BL. Regional quantitative histological variations in human oral mucosa. *Anat Rec (Hoboken)*. 2015;298:562–578.

29. Xiong X, Wu T, He S. Physical forces make rete ridges in oral mucosa. *Med Hypotheses*. 2013;81:883–886.

30. Liao YH, Kuo WC, Chou SY, et al. Quantitative analysis of intrinsic skin aging in dermal papillae by in vivo harmonic generation microscopy. *Biomed Opt Express*. 2014;5:3266–3279.

31. Mine S, Fortunel NO, Pageon H, Asselineau D. Aging alters functionally human dermal papillary fibroblasts but not reticular fibroblasts: a new view of skin morphogenesis and aging. *PLoS One*. 2008;3:e4066.

32. Parfitt GJ, Xie Y, Geyfman M, Brown DJ, Jester JV. Absence of ductal hyper-keratinization in mouse age-related meibomian gland dysfunction (ARMGD). *Aging (Albany NY)*. 2013;5:825–834.

33. Yamaguchi M, Kutsuna M, Uno T, Zheng X, Kodama T, Ohashi Y. Marx line: fluorescein staining line on the inner lid as indicator of meibomian gland function. *Am J Ophthalmol*. 2006;141:669–675.

34. Kim JH, Shin YU, Seong M, Cho HY, Kang MH. Eyelid changes related to meibomian gland dysfunction in early middle-aged patients using topical glaucoma medications. *Cornea*. 2018;37:421–425.

35. Knop E, Korb DR, Blackie CA, Knop N. The lid margin is an underestimated structure for preservation of ocular surface health and development of dry eye disease. *Dev Ophthalmol*. 2010;45:108–122.

36. Norn M. Meibomian orifices and Marx's line. Studied by triple vital staining. *Acta Ophthalmol (Copenh)*. 1985;63:698–700.

37. Wang J, Palakuru JR, Aquavella JV. Correlations among upper and lower tear menisci, noninvasive tear break-up time, and the Schirmer test. *Am J Ophthalmol*. 2008;145:795–800.